Magnetic Resonance Imaging 109 (2024) 271–285

Contents lists available at ScienceDirect

Magnetic Resonance Imaging

journal homepage: www.elsevier.com/locate/mri

A fully Bayesian approach for comprehensive mapping of magnitude and phase brain activation in complex-valued fMRI data

Zhengxin Wang [a], Daniel B. Rowe [b], Xinyi Li [a], D. Andrew Brown [a,*]

[a] School of Mathematical and Statistical Sciences, Clemson University, Clemson 29634, SC, USA
[b] Department of Mathematical and Statistical Sciences, Marquette University, Milwaukee 53233, WI, USA

ARTICLE INFO

Keywords:
Gibbs sampling
Parallel computation
Phase analysis
Rowe–Logan
Spike and slab prior
Variable selection

ABSTRACT

Functional magnetic resonance imaging (fMRI) plays a crucial role in neuroimaging, enabling the exploration of brain activity through complex-valued signals. These signals, composed of magnitude and phase, offer a rich source of information for understanding brain functions. Traditional fMRI analyses have largely focused on magnitude information, often overlooking the potential insights offered by phase data. In this paper, we propose a novel fully Bayesian model designed for analyzing single-subject complex-valued fMRI (cv-fMRI) data. Our model, which we refer to as the CV-M&P model, is distinctive in its comprehensive utilization of both magnitude and phase information in fMRI signals, allowing for independent prediction of different types of activation maps. We incorporate Gaussian Markov random fields (GMRFs) to capture spatial correlations within the data, and employ image partitioning and parallel computation to enhance computational efficiency. Our model is rigorously tested through simulation studies, and then applied to a real dataset from a unilateral finger-tapping experiment. The results demonstrate the model's effectiveness in accurately identifying brain regions activated in response to specific tasks, distinguishing between magnitude and phase activation.

1. Introduction

Functional magnetic resonance imaging (fMRI) has become indispensable in a variety of applications ranging from diagnosis of pathological conditions to the investigation of complex physiological processes in the human brain. During acquisition, fMRI inherently generates complex-valued signals characterized by real and imaginary components, and further summarized as magnitude and phase. This complex structure arises from the forward and inverse Fourier transformations executed in the data collection process, which are affected by phase imperfections [1]. These signals may exhibit changes in magnitude, phase, or both over time in response to a stimulus, as shown in Fig. 1.

The magnitude changes in complex-valued fMRI (cv-fMRI) are fundamentally driven by the blood-oxygenation-level-dependent (BOLD) effect, which operates through a cascade of hemodynamic responses. Neuronal activity leads to increased demand of oxygen, so the freshly oxygenated blood fluxes into the active region and displaces deoxygenated blood, leading to an overall increase in the oxygenation level of the blood in that region. These changes in blood oxygenation cause a change in BOLD signal and magnetic susceptibility, affecting the magnitude of MR signal. Thus, the BOLD effect can be considered an indirect measure of neuronal activity, mediated through vascular changes [2,3].

On the other hand, phase changes are influenced not only by the BOLD effect but also by the electrical neuronal activity directly. These neuronal activations generate moving charges, creating localized electromagnetic fields. These induced electromagnetic fields, in turn, influence the phase of the MRI signal. For this reason, the phase changes are able to reveal the aspects of neuronal activity or other phenomena that might be undetected by magnitude-based analyses [5]. Importantly, previous work [6] has illustrated that the complex-valued model, which incorporates phase information, exhibits superior power of detection over the magnitude-only model. By accurately modeling these phase changes, researchers can gain insights into the more direct effects of neuronal activity on the MRI signal, potentially leading to more precise and informative interpretations of fMRI data [7]. This is especially crucial in understanding complex brain functions and improving the accuracy of fMRI in research and clinical applications.

Traditionally, fMRI studies that aim to map brain activity have predominantly focused on analyzing only the magnitude of these MR signals [8,9]. The phase components are frequently disregarded during

* Corresponding author.
E-mail address: ab7@clemson.edu (D.A. Brown).

https://doi.org/10.1016/j.mri.2024.03.029
Received 2 February 2024; Received in revised form 3 March 2024; Accepted 19 March 2024
Available online 26 March 2024

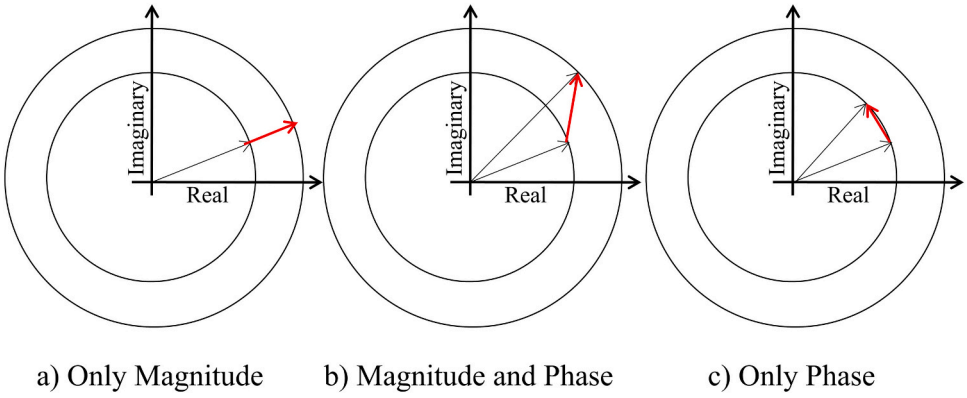

Fig. 1. Illustration of potential changes in complex-valued fMRI time series [4].

the preprocessing steps. The magnitude-only analytical framework has its limitations. The first major limitation is that the omission of phase data results in the underutilization of valuable information that could be pertinent to understanding neurophysiological mechanisms. The second limitation, particularly relevant in studies that employ linear modeling [8,9], concerns the statistical assumptions made during the identification of active voxels (volumetric pixels in the imaging data). In such analyses, the expected BOLD response is usually modeled by the convolution of a "boxcar" binary stimulus function with either a gamma or double-gamma hemodynamic response function (HRF), then a voxel is identified as "active" if the magnitude of its complex-valued fMRI signal shows a statistically significant variation with the expected BOLD response. This practice assumes that the error terms in the models are normally distributed. However, while the original real and imaginary components may follow a normal distribution, the magnitude actually adheres to a Ricean distribution that approximates a normal distribution only when the signal-to-noise ratios (SNRs) are sufficiently large [10,11]. Given that large SNRs are not universally guaranteed in fMRI studies, this statistical assumption of normally distributed error terms becomes less reliable, consequently diminishing the power and reliability of the analysis.

In contrast, emerging research utilizing cv-fMRI data offers a more nuanced and comprehensive approach. By incorporating both the magnitude and phase of the MR signals [6,12–17], or modeling real and imaginary components that both contain magnitude and phase information [18,19], cv-fMRI studies pave the way for the development of more robust and statistically powerful models. These models are better able to handle variations in SNR and can fully exploit the available data, thereby offering potentially deeper and more accurate insights into task-related neuronal activity.

To accurately determine task-related brain activation maps from fMRI signals, fully Bayesian approaches have garnered attention due to their capacity to effectively model both spatial and temporal correlations. However, existing implementations of fully Bayesian methods in fMRI analysis have demonstrated notable shortcomings. For instance, certain studies have applied the fully Bayesian approach only to magnitude data [20,21], leading to underutilization of available data and flawed statistical assumptions as previously discussed. Additionally, others have employed fully Bayesian methods on cv-fMRI data, yet relied on a Cartesian model [22,23], which is limited to identifying active voxels without providing specific insights into the type of activation, be it in terms of magnitude, phase, or a combination of both.

In this paper, we propose a novel fully Bayesian model for mapping brain activity using single-subject cv-fMRI time series. Our model is designed to determine which voxels exhibit significant fMRI signal changes in response to a particular task, specifying the type and strength of these changes. This proposed Bayesian approach for fMRI data analysis is distinctive in its comprehensive utilization of both the real and imaginary components of fMRI data. It is capable of independently predicting different types of activation maps, in terms of magnitude, or phase, or both, capturing spatial correlations, and ensuring computational efficiency.

To effectively capture spatial associations present in cv-fMRI data, our approach incorporates Gaussian Markov random fields [GMRFs; 24]. Moreover, we enhance computational efficiency by employing image partitioning and parallel computation strategies in our Markov chain Monte Carlo [MCMC; 25] algorithms.

The paper is structured as follows: Section 2 introduces our proposed model, its parameters, and brain parcellation strategy. Section 3.1 presents simulation studies and compares our approach with existing methods. In Section 3.2, we apply our model to a real finger-tapping experiment dataset. Section 4 summarizes our findings and suggests future research directions.

2. Material and methods

In this section, we present our model designed for mapping brain activity using cv-fMRI data. Additionally, we introduce the brain parcellation strategy, which facilitates the parallel computation. Following this, we detail the implementation of a GMRF prior that effectively captures the spatial correlations inherent within the fMRI data. Finally, we describe an MCMC algorithm for approximating the posterior distribution of the parameters of interest.

2.1. Model formulation

The polar model of [13] has gained significant attention for modeling complex-valued fMRI data. Originating from the initial formulation with dynamic magnitude and constant phase [6], the model has undergone several iterations [12,14] to arrive at its current version to model both dynamic magnitude and dynamic phase. For a certain voxel v (where $v = 1, \ldots, V$) at time t (where $t = 1, \ldots, T$), its real and imaginary parts of complex-valued fMRI signal, $y_{v,Rt}$ and $y_{v,It}$, can be modeled as:

$$\begin{pmatrix} y_{v,Rt} \\ y_{v,It} \end{pmatrix} = \begin{pmatrix} \rho_{v,t} cos\theta_{v,t} \\ \rho_{v,t} sin\theta_{v,t} \end{pmatrix} + \begin{pmatrix} \varepsilon_{v,Rt} \\ \varepsilon_{v,It} \end{pmatrix}, \quad \begin{pmatrix} \varepsilon_{v,Rt} \\ \varepsilon_{v,It} \end{pmatrix} \sim \mathcal{N}(\mathbf{0}, \sigma_v^2 \mathbf{I}_2),$$

where $\rho_{v,t}$ and $\theta_{v,t}$ are temporally varying magnitude and phase given by:

$$\rho_{v,t} = \beta_{v,0} + x_t \beta_{v,1},$$
$$\theta_{v,t} = \gamma_{v,0} + u_t \gamma_{v,1},$$

where x_t and u_t are the expected BOLD response and neuronal electromagnetic signal, respectively, at time t. Thus, for all time points:

$$\mathbf{y}_v = \begin{pmatrix} \mathbf{A}_R(\boldsymbol{\gamma}_v) \\ \mathbf{A}_I(\boldsymbol{\gamma}_v) \end{pmatrix} \mathbf{X}\boldsymbol{\beta}_v + \boldsymbol{\varepsilon}_v, \quad \boldsymbol{\varepsilon}_v \sim \mathcal{N}\left(\mathbf{0}, \sigma_v^2 \mathbf{I}_{2T}\right), \tag{1}$$

where $\mathbf{y}_v = \left[\left(\mathbf{y}_{v,R}\right)', \left(\mathbf{y}_{v,I}\right)'\right]' \in \mathbb{R}^{2T}$ stacks real and imaginary components of cv-fMRI signal, and $\mathbf{X} = [\mathbf{1}, \mathbf{x}] \in \mathbb{R}^{T\times 2}$ is the design matrix for the magnitude composed of ones and expected BOLD response $\mathbf{x}$. The matrices $\mathbf{A}_R(\boldsymbol{\gamma}_v), \mathbf{A}_I(\boldsymbol{\gamma}_v) \in \mathbb{R}^{T\times T}$ are diagonal as:

$$\mathbf{A}_R(\boldsymbol{\gamma}_v) = \begin{pmatrix} cos\left(\gamma_{v,0} + u_1\gamma_{v,1}\right) & 0 & \cdots & 0 \\ 0 & cos\left(\gamma_{v,0} + u_2\gamma_{v,1}\right) & \cdots & 0 \\ \vdots & \vdots & \ddots & \vdots \\ 0 & 0 & \cdots & cos\left(\gamma_{v,0} + u_t\gamma_{v,1}\right) \end{pmatrix},$$

$$\mathbf{A}_I(\boldsymbol{\gamma}_v) = \begin{pmatrix} sin\left(\gamma_{v,0} + u_1\gamma_{v,1}\right) & 0 & \cdots & 0 \\ 0 & sin\left(\gamma_{v,0} + u_2\gamma_{v,1}\right) & \cdots & 0 \\ \vdots & \vdots & \ddots & \vdots \\ 0 & 0 & \cdots & sin\left(\gamma_{v,0} + u_t\gamma_{v,1}\right) \end{pmatrix},$$

with a more compact form:

$$\mathbf{A}_R(\boldsymbol{\gamma}_v) = diag[cos(\mathbf{U}\boldsymbol{\gamma}_v)], \quad \mathbf{A}_I(\boldsymbol{\gamma}_v) = diag[sin(\mathbf{U}\boldsymbol{\gamma}_v)],$$

where $\mathbf{U} = [\mathbf{1}, \mathbf{u}] \in \mathbb{R}^{T\times 2}$ is the design matrix for the phase composed of ones and neuronal electromagnetic signal $\mathbf{u}$. Therefore, $\boldsymbol{\beta}_v = \left[\beta_{v,0}, \beta_{v,1}\right]' \in \mathbb{R}^2$ and $\boldsymbol{\gamma}_v = \left[\gamma_{v,0}, \gamma_{v,1}\right]' \in \mathbb{R}^2$ are magnitude- and phase-related regression coefficients, respectively. The voxel-specific error term $\boldsymbol{\varepsilon}_v$ follows a multivariate normal distribution with the variance-covariance matrix $\sigma_v^2\mathbf{I}_{2T}$, and a Jeffreys prior can be assigned to σ_v^2 as $p(\sigma_v^2) \propto 1/\sigma_v^2$.

2.2. Brain Parcellation and spatial priors

Spatial correlations are a notable characteristic in fMRI signal data. Given that voxels represent an artificial segmentation of the brain's structure, they frequently display behaviors that are closely aligned with adjacent voxels [4,26–28]. To effectively model these spatial dependencies, it is beneficial to incorporate spatial structuring in the priors of $\boldsymbol{\gamma}_v$ and $\boldsymbol{\beta}_v$ or in the hyperparameters of these priors. Moreover, a strategy of brain parcellation is applied to facilitate the parallel computation.

2.2.1. Brain parcellation

In the study by [21], a technique for brain parcellation was introduced, focusing on the identification of active voxels within individual parcels before integrating these findings into a comprehensive map of brain activity. This approach involves dividing brain images into parcels, each containing 500–1000 voxels. By processing each parcel independently using an identical model and method, the technique allowed for parallel computation, enhancing computational efficiency. Similarly, [23] adopted a comparable approach but differed in their strategy of dividing the brain into parcels of roughly equal geometric size. Both studies demonstrated that this parcellation strategy effectively minimizes edge effects, ensuring that the classification of border voxels in each parcel remains largely unaffected. Following the methodology of [23], we partitioned two- or three-dimensional fMRI images into a set number, G, of parcels, each of approximately equal geometric size. The choice of G is based on empirical judgment, and as indicated by both [21,23], variations within a reasonable range of G do not significantly impact the results.

2.2.2. Prior distributions of $\boldsymbol{\beta}_v$ and $\boldsymbol{\gamma}_v$

For each parcel g (where $g = 1, \ldots, G$) encompassing V_g voxels, we classify a voxel v (where $v = 1, \ldots, V_g$) based on its activity. Specifically, a voxel is classified magnitude-active if $\beta_{v,1} \neq 0$, and phase-active if $\gamma_{v,1} \neq 0$. Adhering to the spike-and-slab prior [29], the model is expressed as follows:

$$\boldsymbol{\beta}_v|\lambda_v, \tau_g^2 \sim \lambda_v\mathcal{N}_2\left(\mathbf{0}, \tau_g^2\mathbf{I}\right) + (1-\lambda_v)\mathcal{N}_2\left(\mathbf{0}, \begin{pmatrix} \tau_g^2 & 0 \\ 0 & 0 \end{pmatrix}\right),$$

$$\boldsymbol{\gamma}_v|\omega_v, \xi_b^2 \sim \omega_v\mathcal{N}_2\left(\mathbf{0}, \xi_g^2\mathbf{I}\right) + (1-\omega_v)\mathcal{N}_2\left(\mathbf{0}, \begin{pmatrix} \xi_g^2 & 0 \\ 0 & 0 \end{pmatrix}\right).$$

In this formulation, $\lambda_v, \omega_v \in \{0, 1\}$ indicate the status of voxel v: $\lambda_v = 1$ for a magnitude-active voxel and $\omega_v = 1$ for a phase-active voxel, with 0 indicating inactivity in respective domains. The parameters τ_g^2 and ξ_g^2 represent parcel-specific variances. These variances are constant for all voxels within a particular parcel but may vary across different parcels, and are assigned a Jeffreys prior, that is, $p\left(\tau_g^2\right) \propto 1/\tau_g^2$ and $p\left(\xi_g^2\right) \propto 1/\xi_g^2$, for $g = 1, \ldots, G$. The prior distributions can be succinctly represented as:

$$\boldsymbol{\beta}_v|\lambda_v, \tau_g^2 \sim \mathcal{N}_2\left(\mathbf{0}, \tau_g^2\boldsymbol{\Lambda}_v\right), \quad \text{where } \boldsymbol{\Lambda}_v = \begin{pmatrix} 1 & 0 \\ 0 & \lambda_v \end{pmatrix},$$

$$\boldsymbol{\gamma}_v|\omega_v, \xi_g^2 \sim \mathcal{N}_2\left(\mathbf{0}, \xi_g^2\boldsymbol{\Omega}_v\right), \quad \text{where } \boldsymbol{\Omega}_v = \begin{pmatrix} 1 & 0 \\ 0 & \omega_v \end{pmatrix}.$$

2.2.3. Spatial prior on λ_v and ω_v

To capture both spatial dependencies and the sparsity of active voxels in brain imaging, we implement a prior distribution for λ_v and ω_v. This approach is rooted in the hypothesis that voxels are more likely to mirror the activity (active/inactive) of their neighboring voxels [8,30], and there should be only a few active voxels across the entire brain from a simple task experiment [31,32]. We employ the sparse spatial generalized linear mixed model (sSGLMM) prior, formulated by [33], and later adopted by [21,23,34]. For voxel v (where $v = 1, \ldots, V_g$) within parcel g (where $g = 1, \ldots, G$), from the perspective of the magnitude, we suppose that:

$$\begin{aligned} \lambda_v|\eta_{\lambda,v} &\overset{iid}{\sim} \mathscr{B}ern\left\{\boldsymbol{\Phi}\left(\psi_\lambda + \eta_{\lambda,v}\right)\right\}, \\ \eta_{\lambda,v}|\boldsymbol{\delta}_{\lambda,g} &\sim \mathcal{N}_1\left(\mathbf{m}_v'\boldsymbol{\delta}_{\lambda,g}, 1\right), \\ \boldsymbol{\delta}_{\lambda,g}|\kappa_{\lambda,g} &\sim \mathcal{N}_q\left\{\mathbf{0}, \left(\kappa_{\lambda,g}\mathbf{M}_g'\mathbf{Q}_g\mathbf{M}_g\right)^{-1}\right\}, \\ \kappa_{\lambda,g} &\sim \mathscr{G}amma(a_\kappa, b_\kappa). \end{aligned}$$

From the perspective of the phase:

$$\begin{aligned} \omega_v|\eta_{\omega,v} &\overset{iid}{\sim} \mathscr{B}ern\left\{\boldsymbol{\Phi}\left(\psi_\omega + \eta_{\omega,v}\right)\right\}, \\ \eta_{\omega,v}|\boldsymbol{\delta}_{\omega,g} &\sim \mathcal{N}_1\left(\mathbf{m}_v'\boldsymbol{\delta}_{\omega,g}, 1\right), \\ \boldsymbol{\delta}_{\omega,g}|\kappa_{\omega,g} &\sim \mathcal{N}_q\left\{\mathbf{0}, \left(\kappa_{\omega,g}\mathbf{M}_g'\mathbf{Q}_g\mathbf{M}_g\right)^{-1}\right\}, \\ \kappa_{\omega,g} &\sim \mathscr{G}amma(a_\kappa, b_\kappa). \end{aligned}$$

In this sSGLMM prior, $\boldsymbol{\Phi}(\cdot)$ represents the cumulative distribution function (CDF) of the standard normal distribution. The terms $\psi_\lambda, \psi_\omega \in \mathbb{R}$ are fixed tuning parameters. The terms $\eta_{\lambda,v}, \eta_{\omega,v} \in \mathbb{R}$ are auxiliary parameters for the probit link functions. Spatial dependencies are modeled through constructs derived from the adjacency matrix $\mathbf{A}_g$ of parcel g. This matrix, $\mathbf{A}_g \in \{0, 1\}^{V_g\times V_g}$, specifies neighborhood relations among voxels, with $\mathbf{A}_{g,uv} = 1$ indicating neighboring voxels u and v (based on user-defined criteria, typically voxels sharing an edge or a corner), and 0 otherwise. The matrix $\mathbf{M}_g \in \mathbb{R}^{V_g\times q}$ is composed of the first q principal eigenvectors of $\mathbf{A}_g$. The row vector $\mathbf{m}_v' \in \mathbb{R}^{1\times q}$ is the v^{th} row of $\mathbf{M}_g$, which is called "synthetic spatial predictors" [34]. The matrix $\mathbf{Q}_g \in \mathbb{R}^{V_g\times V_g}$ is the graph Laplacian, that is, $\mathbf{Q}_g = diag\left(\mathbf{A}_g\mathbf{1}_{V_g}\right) - \mathbf{A}_g$. The vectors $\boldsymbol{\delta}_{\lambda,g}$, $\boldsymbol{\delta}_{\omega,g} \in \mathbb{R}^{q\times 1}$ are spatial random effects, and $\kappa_{\lambda,g}, \kappa_{\omega,g} \in \mathbb{R}$ are spatial smoothing parameters.

This sSGLMM prior captures the spatial correlations by using GMRFs,

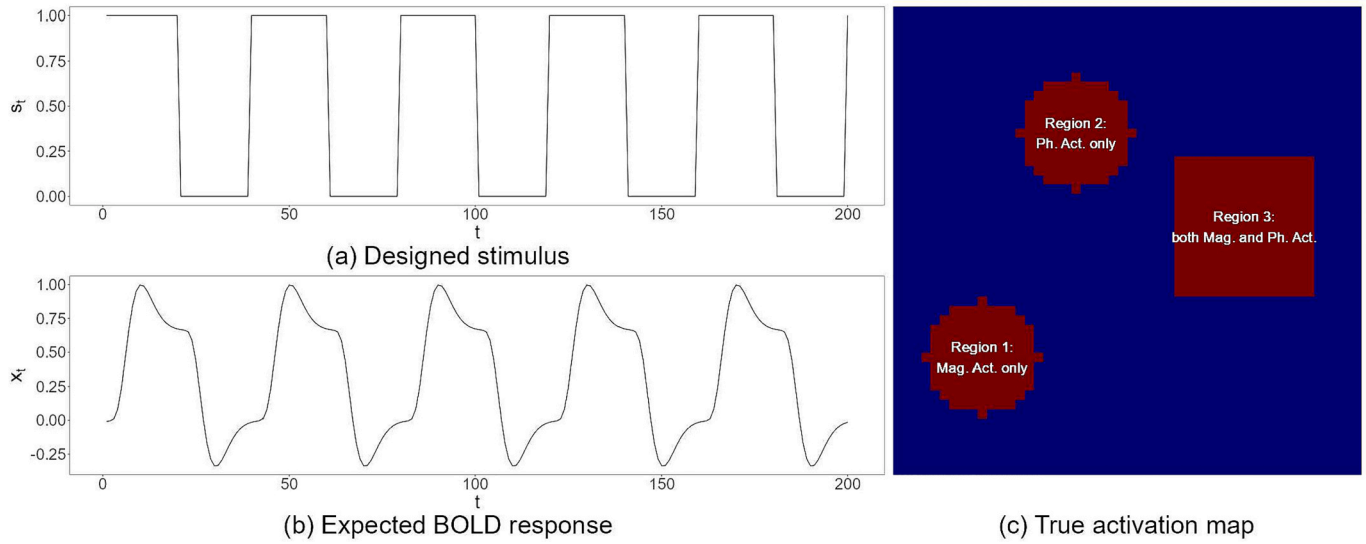

Fig. 2. (a) Designed stimulus; (b) Expected BOLD response; (c) True activation map.

and introduces the sparsity by the selective inclusion of eigenvectors in $\mathbf{M}_g$. Both [21,23] show it is good to capture the spatial correlations in fMRI data that align well with the parcellation strategy. In our simulation studies, the best-performing values of ψ_λ and ψ_ω are pre-selected from a candidate list. For the real data, [21] suggests the initial setting of $\mathbf{\Phi}^{-1}(0.02) = -2.05$, with later adjustments based on previous experiments' active voxel proportions. Moreover, we adopt $q = 5$ (when $V_g \approx 200$), as shown by [34] that q can be remarkably smaller than V_g. The Gamma distribution parameters, $a_\kappa = \frac{1}{2}$ and $b_\kappa = 2000$ are the same for both magnitude and phase, leading to a large mean for $\kappa_{\lambda,g}$ and $\kappa_{\omega,g}$ ($a_\kappa b_\kappa$=1000), minimizing the risk of detecting spurious activity due to noise or other confounding factors.

2.3. MCMC algorithm and posterior distributions

We employ Gibbs sampling to obtain the joint and marginal conditional distributions of parameters of interest. Only the full conditional posterior distribution of $\boldsymbol{\gamma}_v$ is accessed via the Metropolis–Hastings algorithm [35,36], the others follow known and available distributions. Detailed derivations and the required full conditional distributions are provided in the online supplementary material. To assess the convergence of the algorithm, we adopt the fixed-width diagnostic technique suggested by [37]. Convergence is considered achieved when the Monte Carlo Standard Error (MCSE) for all λ_v and ω_v drops below 0.05, leading us to run 10^3 iterations. After discarding the burn-in phase, the means of the sampled parameters are taken as point estimates. If $\widehat{\lambda}_v > 0.925$, the voxel is magnitude-active; if $\widehat{\omega}_v > 0.925$, it is phase-active. [30] proposed the threshold of 0.8722 regarding the significance level $\alpha = 0.05$. Since our approach is similar to a two-step sequential test, we use Bonferroni correction to make $\alpha = 0.05/2 = 0.025$, leading to the adjustment of threshold from 0.8722 to 0.925.

3. Results

3.1. Simulation studies

This section presents two distinct simulation studies. The first study focuses on a single map that comprises three types of active regions: one region is solely magnitude-active, another is solely phase-active, and the third is both magnitude- and phase-active. The second study involves multiple datasets, each containing only one type of activation on their maps. For comparative evaluation, we consider the following models:

- The model proposed by [21], referred to as MO, models magnitude-only data. For a certain voxel v, $v = 1, \ldots, V$, over time T:

$$\mathbf{y}_{v,M} = \mathbf{X}\boldsymbol{\beta}_{v,M} + \boldsymbol{\epsilon}_v, \qquad \boldsymbol{\epsilon}_v \sim \mathcal{N}(\mathbf{0}, \sigma_v^2 \mathbf{I}_T)$$

where $\mathbf{y}_{v,M} \in \mathbb{R}^T$ is the magnitude of complex-valued fMRI signal, and $\mathbf{X} = [\mathbf{1}, \mathbf{x}] \in \mathbb{R}^{T\times 2}$ is the design matrix composed of ones and expected BOLD response $\mathbf{x}$. The vector $\boldsymbol{\beta}_{v,M} = (\beta_{v,M_0}, \beta_{v,M_1})'$ are regression coefficients.

- The model delineated by [23], based on [18]'s Cartesian model and referred to as CV-R&I, models complex-valued data by modeling the real and imaginary components:

$$\mathbf{y}_v = \begin{pmatrix} \mathbf{X} & \mathbf{0} \\ \mathbf{0} & \mathbf{X} \end{pmatrix} \begin{pmatrix} \boldsymbol{\beta}_{v,R} \\ \boldsymbol{\beta}_{v,I} \end{pmatrix} + \boldsymbol{\epsilon}_v, \quad \boldsymbol{\epsilon}_v \sim \mathcal{N}(\mathbf{0}, \sigma_v^2 \mathbf{I}_{2T}),$$

where $\mathbf{y}_v = \left[\left(\mathbf{y}_{v,R}\right)', \left(\mathbf{y}_{v,I}\right)' \right]' \in \mathbb{R}^{2T}$ is the stack of real and imaginary components of cv-fMRI signal. The vectors $\boldsymbol{\beta}_{v,R} = (\beta_{v,R_0}, \beta_{v,R_1})'$ and $\boldsymbol{\beta}_{v,I} = (\beta_{v,I_0}, \beta_{v,I_1})'$ are regression coefficients regarding real and imaginary components of cv-fMRI signal, respectively.

- The model (1), referred to as CV-M&P, is based on [13]'s polar model and models complex-valued data while characterizing magnitude and phase.

All three models adhere to a fully Bayesian approach, employ the sSGLMM spatial prior with brain parcellation strategy, and utilize Gibbs sampling to approximate their respective posterior distributions. The number of parcels G is set to 16 for all models. Other tuning parameters, such as $\psi = \Phi^{-1}(0.35)$ for MO, $\psi = \Phi^{-1}(0.30)$ for CV-R&I, and $\psi = \omega = \Phi^{-1}(0.42)$ for CV-M&P, are predetermined based on their superior performance in prediction accuracy among the range of candidate values. The thresholds for identifying active voxels are set at 0.8722 for MO and CV-R&I, as specified in their work, while CV-M&P employs a threshold of 0.925, in accordance with Section 2.3.

All results are generated by running the code on a custom-built desktop computer with an Intel Core i9-9980XE CPU (3.00GHz, 3001 Mhz, 18 cores, 36 logical processors), NVIDIA GeForce RTX 2080 Ti GPU, 64 GB RAM, and operating on Windows 10 Pro.

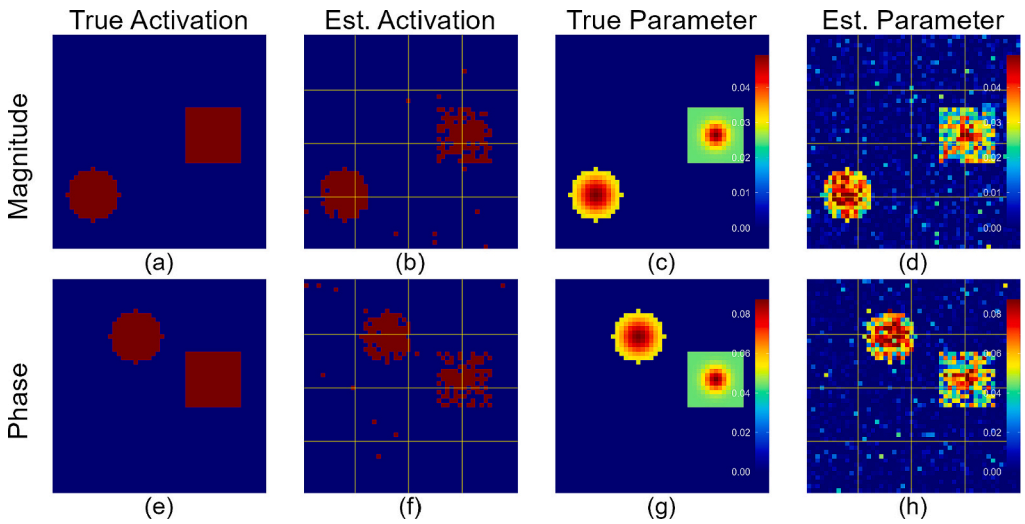

Fig. 3. (a) and (e) are true magnitude and phase activation maps; (b) and (f) are estimated activation maps as derived from CV-M&P; (c) and (g) are true β_1 and γ_1; (d) and (h) are estimated β_1 and γ_1 as derived from CV-M&P.

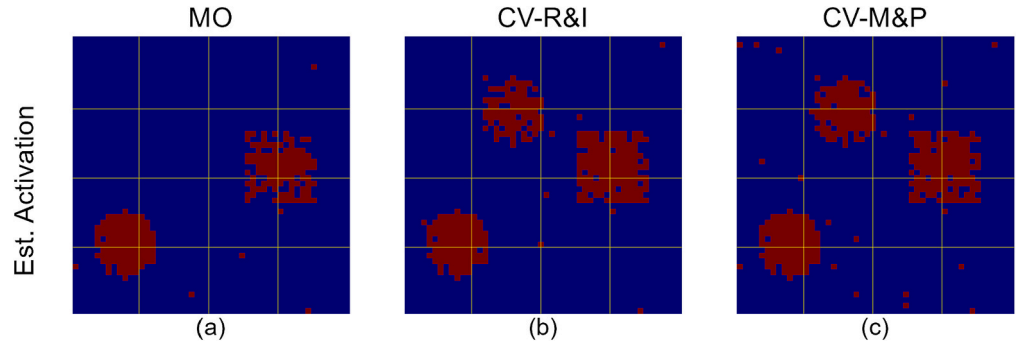

Fig. 4. (a)-(c) are estimated activation maps as derived from MO, CV-R&I, and CV-M&P, respectively.

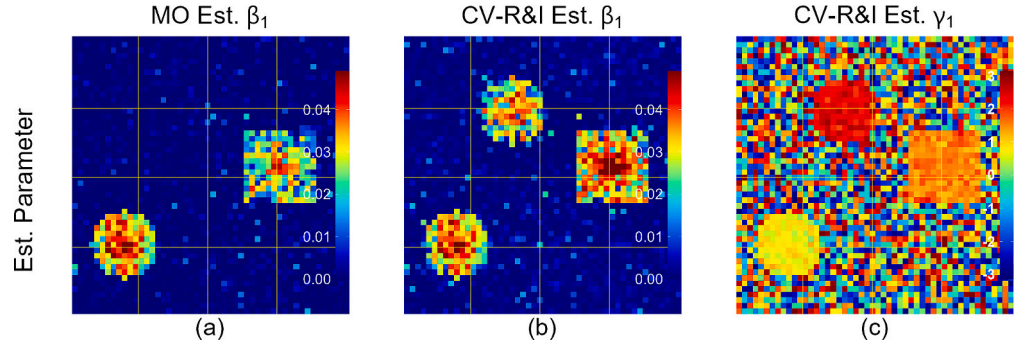

Fig. 5. (a)-(c) are improperly estimated parameters as derived from MO and CV-R&I.

Table 1
Metrics of a single simulated dataset produced by the MO, CV-R&I, and CV-M&P models.

Model	Accuracy	Precision	Recall	F1 Score	AUC	β_1 slope	γ_1 slope	Time (s)
MO	0.9248	0.9726	0.5392	0.6938	0.8910	0.8630	NA	**1.54**
CV-R&I	**0.9688**	**0.9731**	0.8253	0.8931	0.9868	1.0301	33.427	3.93
CV-M&P	0.9680	0.9436	**0.8481**	**0.8933**	**0.9896**	**0.9731**	**0.9462**	17.87

3.1.1. Single simulation

3.1.1.1. Designed stimulus and expected BOLD response. The designed task-related stimulus **S** is a binary signal comprised of five repeated epochs, each spanning 40 time points, resulting in a total duration of $T = 200$ time points. Each epoch features the stimulus being alternately active and inactive, with both states persisting for 20 time points. We

Table 2
Characteristics of true maps.

Map size	Number of active regions	Radius	Shape	Decay rate (ρ)
50 × 50	3	2 to 6	sphere or cube	0 to 0.3

Table 3
Summary of average metrics across 100 simulated datasets produced by the MO, CV-R&I, and CV-M&P models. The values in parentheses are min, max, and standard deviation.

Data Type	Measure	MO	CV-R&I	CV-M&P
Mag. -only	Accuracy	**0.9645**(0.9208, 0.9940, 0.0153)	0.9555(0.9032, 0.9916, 0.0188)	0.9598(0.9132, 0.9900, 0.0160)
	Precision	**0.9647**(0.9157, 0.9917, 0.0164)	0.9601(0.9078, 0.9964, 0.0166)	0.9317(0.8515, 0.9805, 0.0224)
	Recall	**0.7629**(0.6052, 0.9680, 0.0707)	0.6966(0.5263, 0.9406, 0.0840)	0.7534(0.6111, 0.9634, 0.0721)
	F1 Score	**0.8502**(0.7366, 0.9716, 0.0437)	0.8046(0.6741, 0.9515, 0.0557)	0.8311(0.7294, 0.9444, 0.0435)
	AUC	0.9760(0.9485, 0.9991, 0.0107)	0.9605(0.9227, 0.9963, 0.0154)	**0.9793**(0.9605, 0.9983, 0.0081)
	β_1 slope	0.8696(0.7927, 0.9466, 0.0327)	0.8337(0.7451, 0.9356, 0.0406)	**0.9771**(0.9337, 1.0170, 0.0190)
	γ_1 slope	NA	NA	NA
Ph. -only	Accuracy	0.8638(0.7576, 0.9428, 0.0418)	0.9390(0.8696, 0.9848, 0.0234)	**0.9459**(0.8868, 0.9832, 0.0201)
	Precision	0.2102(0.0714, 0.6000, 0.1097)	**0.9481**(0.8829, 0.9862, 0.0207)	0.9192(0.8324, 0.9735, 0.0303)
	Recall	0.0059(0.0017, 0.0201, 0.0034)	0.5718(0.4207, 0.9026, 0.0970)	**0.6481**(0.5146, 0.9090, 0.0881)
	F1 Score	0.0114(0.0034, 0.0373, 0.0065)	0.7088(0.5831, 0.9269, 0.0725)	**0.7569**(0.6456, 0.9225, 0.0604)
	AUC	0.5277(0.4898, 0.6001, 0.0214)	0.9326(0.8844, 0.9930, 0.0237)	**0.9544**(0.9216, 0.9952, 0.0150)
	β_1 slope	NA	NA	NA
	γ_1 slope	NA	39.813(30.031, 45.799, 3.3285)	**0.9439**(0.8744, 1.0271, 0.0289)
Both	Accuracy	0.9644(0.9192, 0.9912, 0.0144)	**0.9835**(0.9616, 0.9984, 0.0071)	0.9769(0.9544, 0.9896, 0.0069)
	Precision	0.9643(0.9017, 0.9892, 0.0146)	**0.9798**(0.9354, 0.9967, 0.0106)	0.9134(0.7870, 0.9617, 0.0294)
	Recall	0.7606(0.6358, 0.9662, 0.0651)	0.8949(0.8216, 0.9925, 0.0362)	**0.9073**(0.8457, 0.9927, 0.0329)
	F1 Score	0.8489(0.7703, 0.9592, 0.0398)	**0.9350**(0.8926, 0.9908, 0.0202)	0.9097(0.8299, 0.9539, 0.0208)
	AUC	0.9763(0.9537, 0.9992, 0.0103)	0.9939(0.9846, 0.9999, 0.0035)	**0.9940**(0.9873, 0.9997, 0.0026)
	β_1 slope	0.8710(0.7879, 0.9789, 0.0321)	1.2346(1.1693, 1.3360, 0.0305)	**0.9843**(0.9365, 1.0316, 0.0183)
	γ_1 slope	NA	26.643(19.307, 30.993, 2.4747)	**0.9534**(0.8958, 1.0146, 0.0253)

model the expected BOLD response **x** by convolving this stimulus with a double-gamma HRF. Illustrations of both the designed stimulus and the expected BOLD response are provided in Fig. 2a and b, respectively, and are consistently used across all our simulation datasets.

3.1.1.2. True activation map and true strength map. The true activation map contains three active regions on a 50 × 50 panel, comprising two circles and one square, each with a radius of five. The exact locations of these regions are depicted in Fig. 2c. We assign distinct types of activation to each region: region 1 exhibits only magnitude activation, region 2 exhibits only phase activation, and region 3 exhibits both magnitude and phase activation, corresponding to the types illustrated in Fig. 1a, c, and b, respectively.

Utilizing the `specifyregion` function in the `neuRosim` library [38] in `R` [39], we initially generate a strength map with decay rates of 0.05, 0.05, and 0.15 for the three regions, respectively. This setup ensures that the central voxel of each active region has a strength of one, diminishing to zero towards the edges at the specified decay rate. For the true magnitude strengths, indicative of voxel response in magnitude to the stimulus, we multiply the strengths in regions 1 and 3 by 0.04909, following [6] who chose that value to mimic the standard deviation in real human data from empirical experience. We nullify the strengths in region 2, as represented in Fig. 3c. Similarly, for the true phase strengths, reflective of voxel response in phase, we multiply the strengths in regions 2 and 3 by a factor of $\pi/36$ and reduce the strengths in region 1 to zero, as illustrated in Fig. 3 g. This methodology ensures that each region's activation profile is accurately mapped according to its designated stimulus response type.

3.1.1.3. Simulating fMRI signals. We then simulate data according to Eq. (2):

$$\begin{aligned} y_{v,Rt} &= (\beta_0 + x_t\beta_{v,1})cos(\gamma_0 + u_t\gamma_{v,1}) + \varepsilon_{v,Rt}, \quad \varepsilon_{v,Rt} \sim \mathcal{N}(0,\sigma^2), \\ y_{v,It} &= (\beta_0 + x_t\beta_{v,1})sin(\gamma_0 + u_t\gamma_{v,1}) + \varepsilon_{v,It}, \quad \varepsilon_{v,It} \sim \mathcal{N}(0,\sigma^2), \end{aligned} \tag{2}$$

where $\beta_0 = 0.4909$, $\gamma_0 = \pi/4$, and $\sigma = 0.04909$ are set constant for all voxels, and x_t is the expected BOLD response **x** from Fig. 2b at time t. It should be noted that we also use $\mathbf{u} = \mathbf{x}$ as the regressor for phase here when generating the data, but it could be its own neuronal electromagnetic signal **u** for the phase in some cases. The signal-to-noise ratio for the magnitude (SNR_{Mag}) is thereby fixed at $\beta_0/\sigma = 10$. The true values of β_1 and γ_1 generated previously in Figs. 3c and 3 g are used, yielding the contrast-to-noise ratios for magnitude (CNR_{Mag}) and phase (CNR_{Ph}) as detailed in Eq. (3):

$$\begin{aligned} CNR_{Mag} &= (max\beta_{v,1})/\sigma = 0.04909/0.04909 = 1, \\ CNR_{Ph} &= (max\gamma_{v,1})/SNR_{Mag} = (\pi/36)/10. \end{aligned} \tag{3}$$

3.1.1.4. Results. Fig. 3 presents both the true and estimated activation maps for magnitude and phase as derived from the CV-M&P model, alongside the corresponding true and estimated parameters β_1 and γ_1. Notably, CV-M&P effectively identifies separate regions that are active in magnitude and phase, and provides proper estimates for the parameters β_1 and γ_1. In the estimated activation maps (Figs. 3b and 3f), the overlap in the predicted active regions corresponds to the square-shaped region 3 in the true map (Fig. 2c), which is characterized by both magnitude and phase activation. When the predicted region 3 is excluded from these estimated maps, the remaining areas align well with the circular regions 1 and 2 in Fig. 2c, representing solely magnitude-active and solely phase-active voxels, respectively.

By synthesizing the estimated activation maps for both magnitude and phase (Figs. 3b and 3f), we construct a composite activation map and compare it against results from MO and CV-R&I. Fig. 4 presents these comparative maps. Performance evaluation reveals that MO fails the competition, primarily due to its inability to detect the phase-only active region 2. Conversely, both CV-R&I and CV-M&P deliver competitive results.

The analysis also extends to comparing the parameter estimates across the three models. As MO and CV-R&I do not explicitly characterize parameters β_1 and γ_1 in their models, we resort to indirect methods for their estimation. For the MO model, we use the estimated slope of the BOLD signal, $\widehat{\beta}_{v,M_1}$, as an estimator for $\beta_{v,1}$, while for CV-R&I, the square root of the sum of squares of the estimated slopes, $\sqrt{(\widehat{\beta}_{v,R_1})^2 + (\widehat{\beta}_{v,I_1})^2}$, serves as an estimator for $\beta_{v,1}$. As for γ_1, MO cannot estimate this parameter due to its limitation to magnitude-only data. In contrast, CV-R&I employs $arctan(\widehat{\beta}_{v,I_1}/\widehat{\beta}_{v,R_1})$ as an estimator for γ_1. These results are illustrated in Fig. 5. Upon examination of Fig. 5a, we observe that while MO's estimated β_1 map appears to closely align with the true β_1 map (Fig. 3c), it still slightly underestimates values in region 3. Similarly, as seen in Fig. 5b, CV-R&I not only falsely estimates the non-existent β_1 in the phase-only active region 2, but also tends to overestimate β_1 in region 3. This overestimation of β_1 in region 3 where

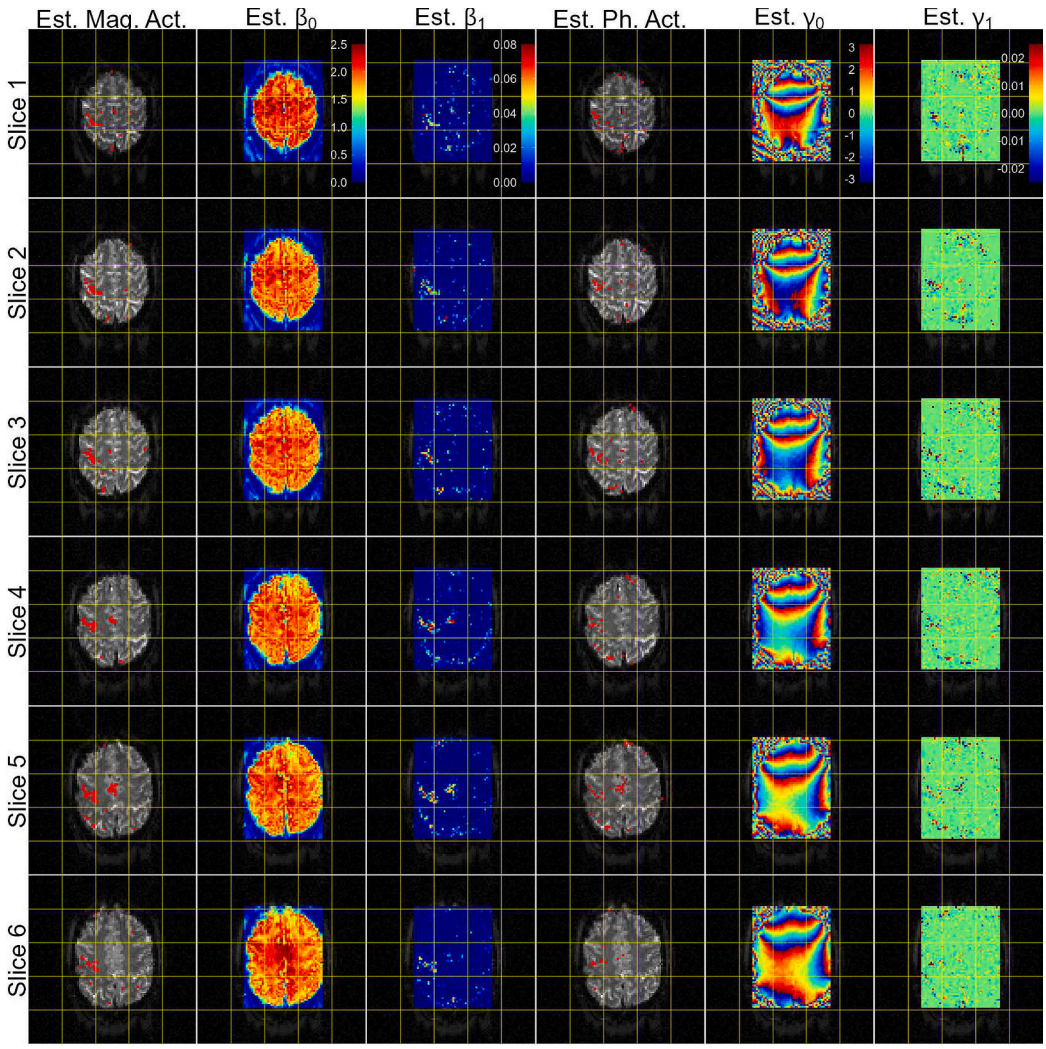

Fig. 6. Estimated magnitude activation, β_0, β_1, phase activation, γ_1, γ_0 maps for a real human brain dataset as derived by the CV-M&P model.

voxels exhibit both magnitude- and phase-active, is consistent with the findings in [23]. Lastly, Fig. 5c reveals the CV-R&I's estimated γ_1 map significantly deviates from the true γ_1 map, as showcased in Fig. 3 g.

The numerical evaluation metrics are summarized in Table 1, where we employ accuracy, precision, recall, F1-score, and the area under the receiver operating characteristic curve (ROC-AUC) to gauge classification performance. We also employ the regression slope between true and estimated parameters to quantify the estimation performance, in which the closer it is to one, the better. In terms of classification, CV-M&P outperforms its counterparts in various key metrics, including recall, F1-score, and AUC. While the margin of superiority may not be pronounced, CV-M&P offers two distinct advantages over its counterparts: it allows for the independent prediction of magnitude and phase activation maps, as shown in Fig. 3b and 3f, while the other two approaches cannot, and provides accurate estimation for both β_1 and γ_1, as the slopes (0.9731 and 0.9462) are close to one. Further evidence from multiple simulation studies, to be discussed in the subsequent section, reinforces these findings.

3.1.1.5. Event-related designs. We consider in this Subsection and in Subsection 3.2 so-called block designs for task fMRI. However, event-related designs are also commonly used [40]. While these designs of course have different design matrices associated with them, our proposed CV-M&P model is able to accommodate them as well. In Appendix B, we conduct a simulation study similar to that presented here, but with an event-related design instead of a block design. The performance of the CV-M&P model is nearly identical to that that which is presented here, thus illustrating the wide applicability of the proposed approach.

3.1.2. Multiple simulations

3.1.2.1. Generating random maps and simulating fMRI signals. We generate 100 random true strength maps using the parameters outlined in Table 2 and the `specifyregion` function. The true strength maps are then scaled by factors of 0.04909 and $\pi/36$ to obtain 100 true β_1 maps and 100 true γ_1 maps, respectively. Using Eq. (2) and the expected BOLD response $\mathbf{x}$ in Fig. 2b, we generate three datasets from each pair of true β_1 and γ_1 maps with the following assignments:

- β_1 present, γ_1 absent (all active voxels are solely magnitude-active)
- β_1 absent, γ_1 present (all active voxels are solely phase-active)
- β_1 present, γ_1 present (all active voxels are both magnitude- and phase-active)

The values for β_0, γ_0, and σ are held constant as specified in Section 3.1.1, with values 0.4909, $\pi/4$, and 0.04909, respectively, resulting in $\mathrm{CNR}_{\mathrm{Mag}} = 1$ and $\mathrm{CNR}_{\mathrm{Ph}} = (\pi/36)/10$. In total, we have 300 datasets for analysis.

3.1.2.2. Results. Table 3 presents the performance metrics for each

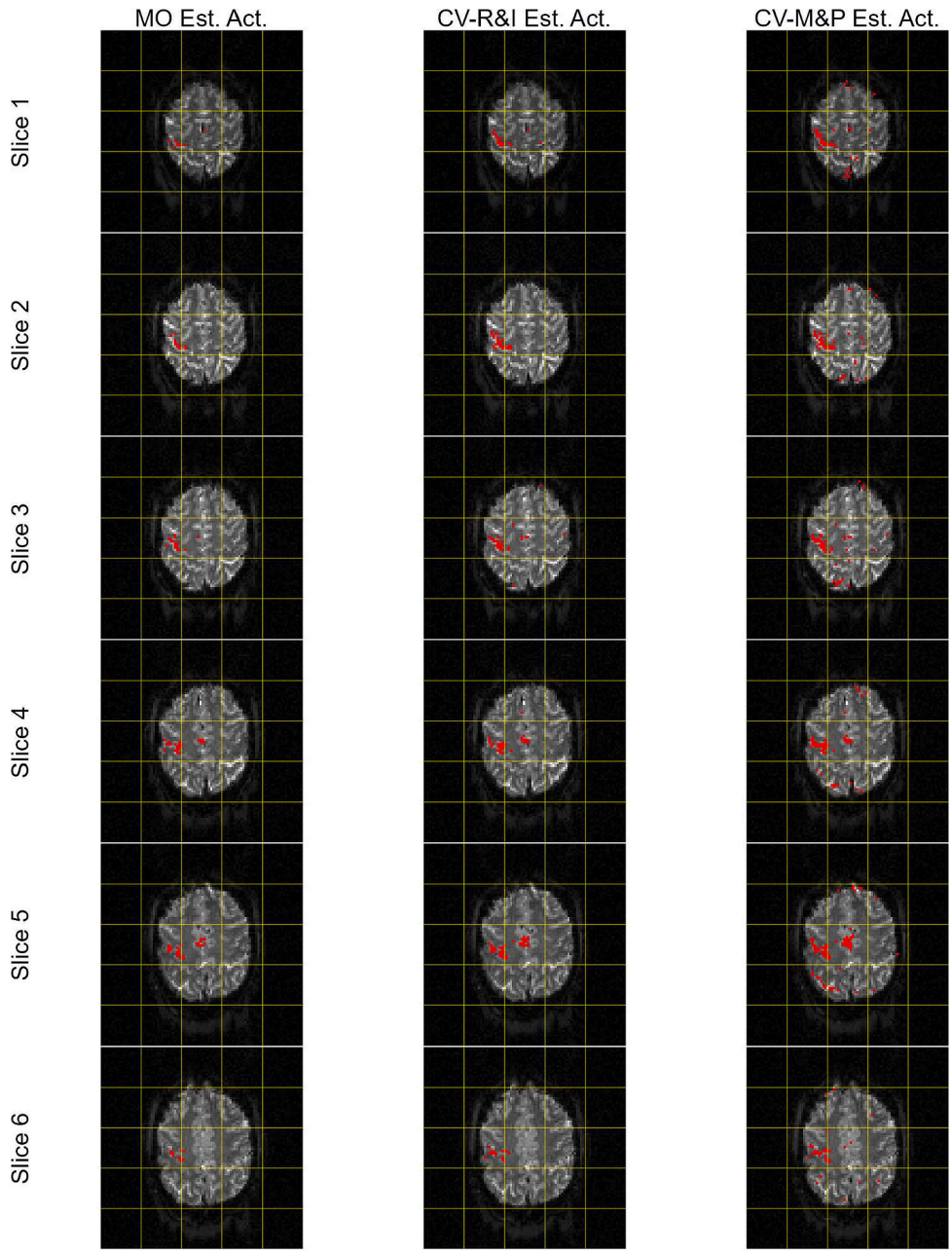

Fig. 7. Estimated activation maps for a real human brain dataset as derived by the MO, CV-R&I, and CV-M&P models.

method across these diverse datasets. In terms of classification, MO delivers superior performance in almost all evaluated metrics for datasets featuring exclusively magnitude-active voxels, which is expected given its design specificity for magnitude-based activity. However, such an assumption of magnitude-only activity is often unrealistic in real-world applications. When considering datasets comprising of solely phase-active voxels, CV-M&P excels in all metrics except precision, thereby establishing its superiority in detecting phase-based activity. For mixed activity involving both magnitude and phase, CV-R&I takes the lead in accuracy, precision, and F1-score metrics, whereas CV-M&P dominates in recall and AUC.

CV-M&P once again stands out with respect to parameter estimation. Specifically, its true vs estimated parameter slopes are close to one when the parameters are present in the simulation, indicating accurate estimations. In contrast, this metric from both MO and CV-R&I deviates from the ideal value of one. As explained by [23], under conditions where all active voxels are solely magnitude-active, the Cartesian model of [18] and the polar model of [13] (CV-R&I and CV-M&P, respectively) are approximately equivalent. Hence, in such scenario, CV-R&I can properly estimate β_1, although not surpassing the performance of CV-M&P. In other scenarios, both MO and CV-R&I fall short, either failing to estimate γ_1 or inaccurately estimating both β_1 and γ_1.

3.2. Analysis of human CV-fMRI data

In this study, we employ the experimental data previously analyzed by [19,22,23]. This dataset originates from a unilateral finger-tapping experiment conducted using a 3.0-Tesla General Electric Signa LX MRI scanner. The experimental design comprises 16.33 epochs, each consisting of alternating periods of 15 s on and 15 s off. Consequently, the total number of time points is $T = 490$, excluding the warm-up phase. The acquired dataset has seven slices, each with dimensions 96×96, and our analysis focuses on the six most active slices. For all examined models, we set the number of parcels $G = 25$. Specific tuning parameters

are fixed based on the experience: for the MO model, $\psi = \Phi^{-1}(0.02)$; for CV-R&I, $\psi = \Phi^{-1}(0.1)$; and for CV-M&P, $\psi = \omega = \Phi^{-1}(0.20)$. The thresholds for identifying active voxels are set to values as follows: 0.8722 for both MO and CV-R&I, and 0.925 for CV-M&P, in alignment with Section 2.3 and the simulation studies.

In Fig. 6, we present the results derived from the CV-M&P model. Distinct patterns are observed: the estimated β_0 maps mirror the patterns of magnitude in the background, the estimated γ_0 maps highlight the phase's transition lines across different color zones, and both the estimated β_1 and γ_1 maps reflect patterns consistent with the estimated magnitude and phase activation maps. Such patterns are indicative of the accuracy of our approach in both classification and estimation.

By integrating the magnitude- and phase-activation maps derived by CV-M&P model, we form comprehensive estimated activation maps. They are subsequently compared with activation maps estimated by MO and CV-R&I models, as shown in Fig. 7, revealing significant alignment. Specifically, the two central and central-left active regions detected by CV-M&P are consistent with the findings reported by [19,22,23]. Furthermore, these regions align with known anatomical areas typically activated during finger-tapping tasks. The central region may correspond to the Primary Motor Cortex (M1) or Supplementary Motor Area (SMA), both of which play pivotal roles in voluntary movement and motor planning [41,42]. Adjacently, the central-left region might represent the Primary Somatosensory Cortex (S1) or the Posterior Parietal Cortex, responsible for tactile sensory information processing and sensory-motor integration, respectively [43]. Notably, beyond these well-established regions, CV-M&P uncovers additional active regions at the posterior of the brain. These could be caused by brain motion during the data collection.

In terms of computational efficiency, MO, CV-R&I, and CV-M&P required 12.32 s, 32.59 s, and 910.20 s, respectively, to complete 10^3 iterations. Despite CV-M&P's computational demand and increased execution time, its drawbacks are mitigated by its potential for scalability. As highlighted in the works of [21,23], the employment of a brain parcellation strategy along with the sSGLMM spatial prior has minimal effects on the prediction results, as long as the total parcel number G is in a reasonable range. Given that this dataset can be further divided into more parcels for parallel processing, and considering our computational resources are currently limited to 16 CPU cores, the computational efficiency of the CV-M&P model can be substantially improved.

4. Discussion

Throughout our investigations on both simulated and real human datasets, the CV-M&P model consistently demonstrates its capability to precisely identify voxels that exhibit significant reactions to stimuli, whether in magnitude, in phase, or in a combination of both. Comparing with the polar model of [13] that uses hypothesis testing approaches [6,12–17], our fully Bayesian framework can capture the spatial correlations of fMRI data, and therefore improve the model flexibility. On the other hand, comparing with other fully Bayesian approaches, but based on the Cartesian model [18,22,23], our CV-M&P model rectifies the constraints inherent in the Cartesian models, which can detect active voxels but remains ambiguous about the exact type of the activation [16]. Moreover, the CV-M&P model excels in providing precise parameter estimates, offering a more nuanced framework for delineating brain activation patterns in task-based fMRI analyses.

There are multiple avenues for advancing this research. These include the exploration of more complex models that account for temporal correlations, models that fit the non-circular data wherein the real and imaginary components of the signal are correlated, and efforts aimed at optimizing computational efficiency. Further, the equal-sized or equal-volume parcellation strategies have shown good empirical performance [21,23]. However, the reasons for this behavior have not been thoroughly investigated. We defer this to future work.

Lastly, we remark that the model proposed in this paper is intended for and motivated by task-based fMRI studies. A large number of fMRI studies conducted now are with resting state fMRI [rsfMRI; [44]]. As rsfMRI is primarily concerned with learning networks and connectivity, rather than voxel- or ROI-specific task-related changes in signal, there would need to be fundamental changes to what we propose here to make it appropriate for such studies. We feel that extending our proposed work or otherwise thoroughly investigating the role of both magnitude and phase in the detection of resting-state connectivity is an avenue worth exploring. This could perhaps be done by following the work of [45], who studied correlations of complex-valued time series collected in cv-fMRI. We leave such research to future investigation.

Author statement

The authors of the manuscript titled, "A fully Bayesian approach for comprehensive mapping of magnitude and phase brain activation in complex-valued fMRI data," hereby declare no competing interests.

CRediT authorship contribution statement

Zhengxin Wang: Writing – original draft, Visualization, Software, Methodology, Investigation, Formal analysis, Data curation, Conceptualization. **Daniel B. Rowe:** Writing – review & editing, Supervision, Methodology, Conceptualization. **Xinyi Li:** Writing – review & editing, Supervision. **D. Andrew Brown:** Writing – review & editing, Supervision, Project administration, Methodology.

Acknowledgements

We thank the Editor, an Associate Editor, and two anonymous referees for their comments that improved this work. This research is supported by the National Institute of General Medical Sciences of the National Institutes of Health under award number P20GM139769 (X. Li), and National Science Foundation awards DMS-2210658 (X. Li) and DMS-2210686 (D. A. Brown). The content is solely the responsibility of the authors and does not necessarily represent the official views of the National Institutes of Health or the National Science Foundation.

Appendix A. Conditional Posterior Distributions for Gibbs Sampling

We need the full conditional posterior distributions of

$$\boldsymbol{\beta}_v, \lambda_v, \boldsymbol{\gamma}_v, \omega_v, \sigma_v^2, \tau_g^2, \xi_g^2, \eta_{\lambda,v}, \boldsymbol{\delta}_{\lambda,g}, \kappa_{\lambda,g}, \eta_{\omega,v}, \boldsymbol{\delta}_{\omega,g}, \kappa_{\omega,g}$$

for the Gibbs sampling. All derivations will omit the subscript of g (parcel index) from the parcel-level parameters $\tau_g^2, \xi_g^2, \boldsymbol{\delta}_{\lambda,g}, \kappa_{\lambda,g}, \boldsymbol{\delta}_{\omega,g}, \kappa_{\omega,g}$, since all parcels run the algorithm identically.

A.1. Full conditional distributions of λ_v and ω_v

The full conditional distribution of λ_v (is)

$$\pi\left(\lambda_v|\mathbf{y}_r^v,\boldsymbol{\beta}_v,\boldsymbol{\gamma}_v,\omega_v,\sigma_v^2,\tau^2,\xi^2,\eta_{\lambda,v}\right)=\mathscr{B}ern(P_{\lambda_v}),$$

where

$$\begin{aligned}P_{\lambda_v}&=p\left(\lambda_v=1|\mathbf{y}_r^v,\boldsymbol{\beta}_v,\boldsymbol{\gamma}_v,\omega_v,\sigma_v^2,\tau^2,\xi^2,\eta_{\lambda,v}\right)\\&=\frac{p\left(\lambda_v=1|\eta_{\lambda,v}\right)}{p\left(\lambda_v=1|\eta_{\lambda,v}\right)+\frac{L_0}{L_1}\cdot p\left(\lambda_v=0|\eta_{\lambda,v}\right)}\\&=\frac{\boldsymbol{\Phi}\left(\psi_\lambda+\eta_{\lambda,v}\right)}{\boldsymbol{\Phi}\left(\psi_\lambda+\eta_{\lambda,v}\right)+\frac{L_0}{L_1}\cdot\left[1-\boldsymbol{\Phi}\left(\psi_\lambda+\eta_{\lambda,v}\right)\right]},\end{aligned}$$

and L_0 and L_1 are the joint densities of $\mathbf{y}_v,\boldsymbol{\beta}_v,\lambda_v,\boldsymbol{\gamma}_v,\omega_v,\sigma_v^2,\tau^2,\xi^2$ given $\lambda_v=0$ and $\lambda_v=1$. Let L be such joint density, that is,

$$L=p\left(\mathbf{y}_v,\boldsymbol{\beta}_v,\lambda_v,\boldsymbol{\gamma}_v,\omega_v,\sigma_v^2,\tau^2,\xi^2\right)\propto p\left(\mathbf{y}_v|\boldsymbol{\beta}_v,\lambda_v,\boldsymbol{\gamma}_v,\omega_v,\sigma_v^2\right)p\left(\boldsymbol{\beta}_v|\lambda_v,\tau^2\right).$$

Define:

$$\mathbf{A}_v=\begin{pmatrix}\mathbf{C}_v\\\mathbf{S}_v\end{pmatrix},\quad\text{where }\mathbf{C}_v=diag[cos(\mathbf{U}\boldsymbol{\Omega}_v\boldsymbol{\gamma}_v)\,],\quad\mathbf{S}_v=diag[sin(\mathbf{U}\boldsymbol{\Omega}_v\boldsymbol{\gamma}_v)\,],$$

(Note, $\mathbf{A}_v$ is orthogonal, i.e., $\mathbf{A}_v^{'}\mathbf{A}_v=\mathbf{I}_{2T}$.), then,

$$\begin{aligned}&p\left(\mathbf{y}_v|\boldsymbol{\beta}_v,\lambda_v,\boldsymbol{\gamma}_v,\omega_v,\sigma_v^2\right)\\&\quad=\left(2\pi\sigma_v^2\right)^{-\frac{2T}{2}}exp\left\{-\frac{1}{2\sigma_v^2}(\mathbf{y}_v-\mathbf{A}_v\mathbf{X}\boldsymbol{\Lambda}_v\boldsymbol{\beta}_v)^{'}(\mathbf{y}_v-\mathbf{A}_v\mathbf{X}\boldsymbol{\Lambda}_v\beta_v)\right\}\\&=\left(2\pi\sigma_v^2\right)^{-\frac{2T}{2}}exp\left\{-\frac{1}{2\sigma_v^2}\left[\mathbf{y}_v^{'}\mathbf{y}_v-2(\mathbf{A}_v\mathbf{X}\boldsymbol{\Lambda}_v\beta_v)^{'}\mathbf{y}_v+(\boldsymbol{\Lambda}_v\boldsymbol{\beta}_v)^{'}\mathbf{X}^{'}\mathbf{X}\boldsymbol{\Lambda}_v\beta_v\right]\right\},\end{aligned}$$

and

$$p\left(\boldsymbol{\beta}_v|\lambda_v,\tau^2\right)=\left(2\pi\tau^2\right)^{-\frac{1+\lambda_v}{2}}exp\left\{-\frac{1}{2\tau^2}\boldsymbol{\beta}_v^{'}\boldsymbol{\Lambda}_v\boldsymbol{\beta}_v\right\}.$$

Thus,

$$L\propto\left(2\pi\tau^2\right)^{-\frac{1+\lambda_v}{2}}exp\left\{-\frac{1}{2\sigma_v^2}\left[-2(\mathbf{A}_v\mathbf{X}\boldsymbol{\Lambda}_v\boldsymbol{\beta}_v)^{'}\mathbf{y}_v+(\boldsymbol{\Lambda}_v\boldsymbol{\beta}_v)^{'}\mathbf{X}^{'}\mathbf{X}\boldsymbol{\Lambda}_v\boldsymbol{\beta}_v\right]-\frac{1}{2\tau^2}\boldsymbol{\beta}_v^{'}\boldsymbol{\Lambda}_v\boldsymbol{\beta}_v\right\}.$$

Let $\mathbf{a}_v$ be the flattened version of $\mathbf{A}_v$, that is, $\mathbf{a}_v$ is a $2T\times1$ vector as

$$\mathbf{a}_v=\mathbf{A}_v\mathbf{1}_T=\begin{pmatrix}cos(\mathbf{U}\boldsymbol{\Omega}_v\boldsymbol{\gamma}_v)\\sin(\mathbf{U}\boldsymbol{\Omega}_v\boldsymbol{\gamma}_v)\end{pmatrix}$$

Also, define $\mathbf{x}_{(2)}$ as the second column of $\mathbf{X}$, thus, $\mathbf{x}_{(2)}$ is a $T\times1$ vector of expected BOLD response; define $\mathbf{x}_{(2)}^{*}=\begin{pmatrix}\mathbf{x}_{(2)}\\\mathbf{x}_{(2)}\end{pmatrix}$ as a $2T\times1$ vector to match the dimension, then,

$$\frac{L_0}{L_1}=\frac{L|_{\lambda_v=0}}{L|_{\lambda_v=1}}$$

$$=\left(2\pi\tau^2\right)^{\frac{1}{2}}exp\left\{-\frac{1}{2\sigma_v^2}\left[2\beta_{v,1}\left(\mathbf{x}_{(2)}^{*}\odot\mathbf{a}_v\right)^{'}\mathbf{y}_v-2\beta_{v,0}\beta_{v,1}\mathbf{x}_{(2)}^{'}\mathbf{1}_T-\beta_{v,1}^2\mathbf{x}_{(2)}^{'}\mathbf{x}_{(2)}\right]+\frac{1}{2\tau^2}\beta_{v,1}^2\right\}.$$

We flatten $\mathbf{A}_v$ and use Hadamard product $\odot$ here to lessen the computational burden. Similarly, the full conditional distribution of ω_v is

$$\pi\left(\omega_v|\mathbf{y}_r^v,\boldsymbol{\beta}_v,\lambda_v,\gamma_v,\sigma_v^2,\tau^2,\xi^2,\eta_v\right)=\mathscr{B}ern(P_{\omega_v}),$$

where

$$P_{\omega_v}=\frac{\boldsymbol{\Phi}\left(\psi_\omega+\eta_{\omega,v}\right)}{\boldsymbol{\Phi}\left(\psi_\omega+\eta_{\omega,v}\right)+\frac{L_0}{L_1}\left[1-\boldsymbol{\Phi}\left(\psi_\omega+\eta_{\omega,v}\right)\right]},$$

where

$$L\propto\left(2\pi\xi^2\right)^{-\frac{1+\omega_v}{2}}exp\left\{\frac{1}{\sigma_v^2}(\mathbf{A}_v\mathbf{X}\boldsymbol{\Lambda}_v\boldsymbol{\beta}_v)^{'}\mathbf{y}_v-\frac{1}{2\xi^2}\boldsymbol{\gamma}_v^{'}\boldsymbol{\Omega}_v\boldsymbol{\gamma}_v\right\},$$

and

$$\frac{L_0}{L_1}=\frac{L|_{\omega_v=0}}{L|_{\omega_v=1}}$$

$$=\left(2\pi\xi^2\right)^{\frac{1}{2}}exp\left\{\frac{1}{\sigma_v^2}\left[\left(\mathbf{A}_v|_{\omega_v=0}-\mathbf{A}_v|_{\omega_v=1}\right)\mathbf{X}\boldsymbol{\Lambda}_v\boldsymbol{\beta}_v\right]^{'}\mathbf{y}_v+\frac{1}{2\xi^2}\gamma_{v,1}^2\right\}.$$

Keep simplifying it, when $\lambda_v=0$,

$$\frac{L_0}{L_1}=\left(2\pi\xi^2\right)^{\frac{1}{2}}exp\left\{\frac{1}{\sigma_v^2}\beta_{v,0}\left(\mathbf{a}_v|_{\omega_v=0}-\mathbf{a}_v|_{\omega_v=1}\right)^{'}\mathbf{y}_v+\frac{1}{2\xi^2}\gamma_{v,1}^2\right\}.$$

When $\lambda_v=1$,

$$\frac{L_0}{L_1}=\left(2\pi\xi^2\right)^{\frac{1}{2}}exp\left\{\frac{1}{\sigma_v^2}\left[\left(\beta_{v,0}\mathbf{1}_{2T}+\beta_{v,1}\mathbf{x}_{(2)}^{*}\right)\odot\left(\mathbf{a}_v|_{\omega_v=0}-\mathbf{a}_v|_{\omega_v=1}\right)\right]^{'}\mathbf{y}_v+\frac{1}{2\xi^2}\gamma_{v,1}^2\right\}.$$

A.2. Full conditional distribution of β_v

When $\lambda_v=1$, the full conditional distribution of β_v is

$$\pi\left(\boldsymbol{\beta}_v|\mathbf{y}_v,\lambda_v=1,\boldsymbol{\gamma}_v,\omega_v,\sigma_v^2,\tau^2,\xi^2\right)$$
$$\propto p\left(\mathbf{y}_v,\boldsymbol{\beta}_v,\lambda_v=1,\boldsymbol{\gamma}_v,\omega_v,\sigma_v^2,\tau^2,\xi^2\right)$$
$$\propto p\left(\mathbf{y}_v|\boldsymbol{\beta}_v,\lambda_v=1,\boldsymbol{\gamma}_v,\omega_v,\sigma_v^2\right)p\left(\boldsymbol{\beta}_v|\lambda_v=1,\tau^2\right)$$
$$\propto exp\left\{-\frac{1}{2\sigma_v^2}(\mathbf{y}_v-\mathbf{A}_v\mathbf{X}\boldsymbol{\beta}_v)^{'}(\mathbf{y}_v-\mathbf{A}_v\mathbf{X}\boldsymbol{\beta}_v)\right\}exp\left\{-\frac{1}{2\tau^2}\boldsymbol{\beta}_v^{'}\boldsymbol{\beta}_v\right\}$$
$$\propto exp\left\{-\frac{1}{2}\left[\boldsymbol{\beta}_v^{'}\frac{(\mathbf{A}_v\mathbf{X})^{'}(\mathbf{A}_v\mathbf{X})}{\sigma_v^2}\boldsymbol{\beta}_v-2\boldsymbol{\beta}_v^{'}\frac{(\mathbf{A}_v\mathbf{X})^{'}}{\sigma_v^2}\mathbf{y}_v+\boldsymbol{\beta}_v^{'}\frac{1}{\tau^2}\boldsymbol{\beta}_v\right]\right\}$$
$$=exp\left\{-\frac{1}{2}\left[\boldsymbol{\beta}_v^{'}\frac{(\mathbf{A}_v\mathbf{X})^{'}(\mathbf{A}_v\mathbf{X})+\frac{\sigma_v^2}{\tau^2}\mathbf{I}}{\sigma_v^2}\boldsymbol{\beta}_v-2\boldsymbol{\beta}_v^{'}\frac{(\mathbf{A}_v\mathbf{X})^{'}}{\sigma_v^2}\mathbf{y}_v\right]\right\}$$
$$=exp\left\{-\frac{1}{2}\left[\boldsymbol{\beta}_v^{'}\frac{\mathbf{X}^{'}\mathbf{X}+\frac{\sigma_v^2}{\tau^2}\mathbf{I}}{\sigma_v^2}\boldsymbol{\beta}_v-2\boldsymbol{\beta}_v^{'}\frac{(\mathbf{A}_v\mathbf{X})^{'}}{\sigma_v^2}\mathbf{y}_v\right]\right\}.$$

Therefore,

$$\pi\left(\boldsymbol{\beta}_v|\mathbf{y}_v,\lambda_v=1,\boldsymbol{\gamma}_v,\omega_v,\sigma_v^2,\tau^2,\xi^2\right)=\mathscr{N}_2\left(\boldsymbol{\mu}_{\beta_v},\Sigma_{\beta_v}\right),$$

where

$$\boldsymbol{\mu}_{\beta_v}=\left(\mathbf{X}^{'}\mathbf{X}+\frac{\sigma_v^2}{\tau^2}\mathbf{I}\right)^{-1}(\mathbf{A}_v\mathbf{X})^{'}\mathbf{y}_v,$$
$$\Sigma_{\beta_v}=\sigma_v^2\left(\mathbf{X}^{'}\mathbf{X}+\frac{\sigma_v^2}{\tau^2}\mathbf{I}\right)^{-1},$$

where $\mathbf{A}_v\mathbf{X}$ can be calculated as $\left[\mathbf{a}_v,\mathbf{x}_{(2)}^{*}\odot\mathbf{a}_v\right]$ for faster computation. When $\lambda_v=0$, it's easy to show:

$$\pi\left(\boldsymbol{\beta}_{v,0}|\mathbf{y}_v,\lambda_v=0,\boldsymbol{\gamma}_v,\omega_v,\sigma_v^2,\tau^2,\xi^2\right)=\mathscr{N}\left(\frac{(\mathbf{A}_v\mathbf{1}_T)^{'}\mathbf{y}_v}{T+\frac{\sigma_v^2}{\tau^2}},\frac{\sigma_v^2}{T+\frac{\sigma_v^2}{\tau^2}}\right),$$

and $\boldsymbol{\beta}_{v,1}=0$ with probability 1, where $\mathbf{A}_v\mathbf{1}_T$ is just $\mathbf{a}_v$.

A.3. Sampling $\boldsymbol{\gamma}_v$

We apply Metropolis-Hastings algorithm to sample $\boldsymbol{\gamma}_v$. A random walk proposal,

$$\boldsymbol{\gamma}_v^*|\boldsymbol{\gamma}_v \sim \mathcal{N}_2\left(\boldsymbol{\Omega}_v\boldsymbol{\gamma}_v, \quad \boldsymbol{\Omega}_v^{'}\Sigma_{\gamma_v}\boldsymbol{\Omega}_v\right),$$

is used, where $\boldsymbol{\gamma}_v^*$ and $\boldsymbol{\gamma}_v$ are proposed parameter and current state, respectively, and Σ_{γ_v} is a tuning parameter. We use the current indicator of phase status, $\boldsymbol{\Omega}_v$, to secure it proposes $\boldsymbol{\gamma}_v^* = \begin{pmatrix} \gamma_{v,0}^* \neq 0 \\ \gamma_{v,1}^* = 0 \end{pmatrix}$ when the phase is inactive. Let $p_{\gamma_v}(\cdot)$ be the proposal density, then the acceptance ratio is

$$\begin{aligned} r_{\gamma_v} &= \frac{\pi\left(\boldsymbol{\gamma}_v^*|\mathbf{y}_v, \boldsymbol{\beta}_v, \lambda_v, \omega_v, \sigma_v^2, \tau^2, \xi^2\right) p_{\gamma_v}\left(\boldsymbol{\gamma}_v|\boldsymbol{\gamma}_v^*\right)}{\pi\left(\boldsymbol{\gamma}_v|\mathbf{y}_v, \boldsymbol{\beta}_v, \lambda_v, \omega_v, \sigma_v^2, \tau^2, \xi^2\right) p_{\gamma_v}\left(\boldsymbol{\gamma}_v^*|\boldsymbol{\gamma}_v\right)} \\ &= \frac{p\left(\mathbf{y}_v|\boldsymbol{\beta}_v, \lambda_v, \boldsymbol{\gamma}_v^*, \omega_v, \sigma_v^2\right) p\left(\boldsymbol{\gamma}_v^*|\omega_v, \xi^2\right)}{p\left(\mathbf{y}_v|\boldsymbol{\beta}_v, \lambda_v, \boldsymbol{\gamma}_v, \omega_v, \sigma_v^2\right) p\left(\boldsymbol{\gamma}_v|\omega_v, \xi^2\right)}, \end{aligned}$$

where

$$\begin{aligned} p\left(\mathbf{y}_v|\boldsymbol{\beta}_v, \lambda_v, \boldsymbol{\gamma}_v, \omega_v, \sigma_v^2\right) &\propto exp\left\{ -\frac{1}{2\sigma_v^2}(\mathbf{y}_v - \mathbf{A}_v\mathbf{X}\boldsymbol{\Lambda}_v\boldsymbol{\beta}_v)^{'}(\mathbf{y}_v - \mathbf{A}_v\mathbf{X}\boldsymbol{\Lambda}_v\boldsymbol{\beta}_v) \right\} \\ &\propto exp\left\{ \frac{1}{\sigma_v^2}(\mathbf{A}_v\mathbf{X}\boldsymbol{\Lambda}_v\boldsymbol{\beta}_v)^{'}\mathbf{y}_v \right\}, \\ p\left(\boldsymbol{\gamma}_v|\omega_v, \xi^2\right) &\propto exp\left\{ -\frac{1}{2\xi^2}\boldsymbol{\gamma}_v^{'}\boldsymbol{\Omega}_v\boldsymbol{\gamma}_v \right\}. \end{aligned}$$

Simplify the ratio, when $\lambda_v = 0$,

$$r_{\gamma_v} = exp\left\{ \frac{1}{\sigma_v^2}\beta_{v,0}\left(\mathbf{a}_v\big|_{\gamma_v=\gamma_v^*} - \mathbf{a}_v\big|_{\gamma_v=\gamma_v}\right)^{'}\mathbf{y}_v - \frac{1}{2\xi^2}\left(\gamma_{v,0}^{*,2} - \gamma_{v,0}^2\right) \right\}.$$

When $\lambda_v = 1$,

$$r_{\gamma_v} = exp\left\{ \frac{1}{\sigma_v^2}\left[\left(\beta_{v,0}\mathbf{1}_{2T} + \beta_{v,1}\mathbf{x}_{(2)}^*\right) \odot \left(\mathbf{a}_v\big|_{\gamma_v=\gamma_v^*} - \mathbf{a}_v\big|_{\gamma_v=\gamma_v}\right)\right]^{'}\mathbf{y}_v - \frac{1}{2\xi^2}\left(\boldsymbol{\gamma}_v^{*'}\boldsymbol{\gamma}_v^* - \boldsymbol{\gamma}_v^{'}\boldsymbol{\gamma}_v\right) \right\}.$$

We generate a dummy variable $d_{\gamma_v} \sim \mathcal{U}(0,1)$, and if $d_{\gamma_v} < r_{\gamma_v}$, we update γ_v by γ_v^*, otherwise remain γ_v.

A.4. Full conditional distribution of σ_v^2

Assigning a Jeffreys prior, $p(\sigma_v^2) \propto 1/\sigma_v^2$, we have:

$$\pi\left(\sigma_v^2|\mathbf{y}_v, \cdot\right) = \mathcal{IG}\left(\frac{2T}{2}, \quad \frac{1}{2}(\mathbf{y}_v - \mathbf{A}_v\mathbf{X}\boldsymbol{\Lambda}_v\boldsymbol{\beta}_v)^{'}(\mathbf{y}_v - \mathbf{A}_v\mathbf{X}\boldsymbol{\Lambda}_v\boldsymbol{\beta}_v)\right).$$

Again, to save computational time, $\mathbf{A}_v\mathbf{X}\boldsymbol{\Lambda}_v\boldsymbol{\beta}_v$ can be calculated as $\beta_{v,0}\mathbf{a}_v$ when $\lambda_v = 0$, or $\left(\beta_{v,0}\mathbf{1}_{2T} + \beta_{v,1}\mathbf{x}_{(2)}^*\right) \odot \mathbf{a}_v$ when $\lambda_v = 1$.

A.5. Full conditional distributions of τ^2 and ξ^2

The full conditional distribution of τ^2 should be related to all voxels' β_0's and magnitude-active voxels' β_1's. Assigning a Jeffreys prior, $p(\tau^2) \propto 1/\tau^2$, we have:

$$\pi\left(\tau^2|\mathbf{y}_v, \cdot\right) = \mathcal{IG}\left(\frac{1}{2}\sum_{v=1}^{V}\mathbf{1}_2^{'}\boldsymbol{\Lambda}_v\mathbf{1}_2, \quad \frac{1}{2}\sum_{v=1}^{V}\boldsymbol{\beta}_v^{'}\boldsymbol{\Lambda}_v\boldsymbol{\beta}_v\right).$$

Equivalently,

$$\pi\left(\tau^2|\mathbf{y}_v, \cdot\right) = \mathcal{IG}\left(\frac{1}{2}\left(V + \sum_{v=1}^{V}\lambda_v\right), \quad \frac{1}{2}\sum_{v=1}^{V}\left[\beta_{v,0}^2 + \left(\lambda_v\beta_{v,1}\right)^2\right]\right).$$

Similarly, the full conditional distribution of ξ^2 should be related to all voxels' γ_0's and phase-active voxels' γ_1's, that is,

$$\pi\left(\xi^2|\mathbf{y}_v, \cdot\right) = \mathcal{IG}\left(\frac{1}{2}\sum_{v=1}^{V}\mathbf{1}_2^{'}\boldsymbol{\Omega}_v\mathbf{1}_2, \quad \frac{1}{2}\sum_{v=1}^{V}\boldsymbol{\gamma}_v^{'}\boldsymbol{\Omega}_v\boldsymbol{\gamma}_v\right).$$

Equivalently,

$$\pi\left(\xi^2|\mathbf{y}_v, \cdot\right) = \mathcal{IG}\left(\frac{1}{2}\left(V + \sum_{v=1}^{V}\omega_v\right), \quad \frac{1}{2}\sum_{v=1}^{V}\left[\gamma_{v,0}^2 + \left(\omega_v\gamma_{v,1}\right)^2\right]\right).$$

A.6. Full conditional distributions of η_v, δ, and κ

Let $\mathbf{Q}_s = \mathbf{M}^{'}\mathbf{Q}\mathbf{M}$. then we follow the supplementary material in [23], we have:

$$\pi(\eta_{\lambda,v}|\lambda_v,\kappa_\lambda)=\begin{cases}\mathscr{TN}\left(0,\ \frac{1}{\kappa_\lambda}\left(1+\mathbf{m}_v'\mathbf{Q}_s^{-1}\mathbf{m}_v\right),\ 0,\ \infty\right) & \text{if } \lambda_v=1\\ \mathscr{TN}\left(0,\ \frac{1}{\kappa_\lambda}\left(1+\mathbf{m}_v'\mathbf{Q}_s^{-1}\mathbf{m}_v\right),\ -\infty,\ 0\right) & \text{if } \lambda_v=0\end{cases},$$

$$\pi(\eta_{\omega,v}|\omega_v,\kappa_\omega)=\begin{cases}\mathscr{TN}\left(0,\ \frac{1}{\kappa_\omega}\left(1+\mathbf{m}_v'\mathbf{Q}_s^{-1}\mathbf{m}_v\right),\ 0,\ \infty\right) & \text{if } \omega_v=1\\ \mathscr{TN}\left(0,\ \frac{1}{\kappa_\omega}\left(1+\mathbf{m}_v'\mathbf{Q}_s^{-1}\mathbf{m}_v\right),\ -\infty,\ 0\right) & \text{if } \omega_v=0\end{cases},$$

where $\mathscr{TN}$ denotes the truncated normal distribution. Let $\boldsymbol{\eta}_\lambda=(\eta_{\lambda,1},\ldots,\eta_{\lambda,V})'$ and $\boldsymbol{\eta}_\omega=(\eta_{\omega,1},\ldots,\eta_{\omega,V})'$, then:

$$\pi(\boldsymbol{\delta}_\lambda|\boldsymbol{\eta}_\lambda,\kappa_\lambda)=\mathscr{N}_q\left(\frac{1}{\kappa_\lambda}(\mathbf{Q}_s+\mathbf{M}'\mathbf{M})^{-1}\mathbf{M}'\boldsymbol{\eta}_\lambda,\ \ \frac{1}{\kappa_\lambda}(\mathbf{Q}_s+\mathbf{M}'\mathbf{M})^{-1}\right),$$

$$\pi(\boldsymbol{\delta}_\omega|\boldsymbol{\eta}_\omega,\kappa_\omega)=\mathscr{N}_q\left(\frac{1}{\kappa_\omega}(\mathbf{Q}_s+\mathbf{M}'\mathbf{M})^{-1}\mathbf{M}'\boldsymbol{\eta}_\omega,\ \ \frac{1}{\kappa_\omega}(\mathbf{Q}_s+\mathbf{M}'\mathbf{M})^{-1}\right).$$

Moreover,

$$\pi(\kappa_\lambda|\boldsymbol{\eta}_\lambda)=\mathscr{G}amma\left(a=\frac{V+1}{2},\quad b=\left[\frac{1}{2}\left(\sum_{v=1}^{V}\frac{\eta_{\lambda,v}^2}{(1+\mathbf{m}_v'\mathbf{Q}_s^{-1}\mathbf{m}_v)}\right)+\frac{1}{2000}\right]^{-1}\right),$$

$$\pi(\kappa_\omega|\boldsymbol{\eta}_\omega)=\mathscr{G}amma\left(a=\frac{V+1}{2},\quad b=\left[\frac{1}{2}\left(\sum_{v=1}^{V}\frac{\eta_{\omega,v}^2}{(1+\mathbf{m}_v'\mathbf{Q}_s^{-1}\mathbf{m}_v)}\right)+\frac{1}{2000}\right]^{-1}\right),$$

where b is the scale.

Appendix B. Event-related fmri simulation study

A simulated event-related fMRI signal is also used to verify the performance of the CV-M&P approach. Fig. B.8a displays the pulse stimulus in the event-related fMRI simulation, which differs from the block stimulus used in the task-related simulation shown in Fig. 2a. Utilizing the same parameters described in Section 3.1.1, we simulate a dataset with three active regions, as depicted in Fig. B.8c. Fig. B.9 presents the estimated maps derived from CV-M&P. The approach's performance is comparable to that observed in the task-related fMRI simulation. That is, it successfully predicted the activation maps individually in terms of magnitude and phase and estimated the parameters properly.

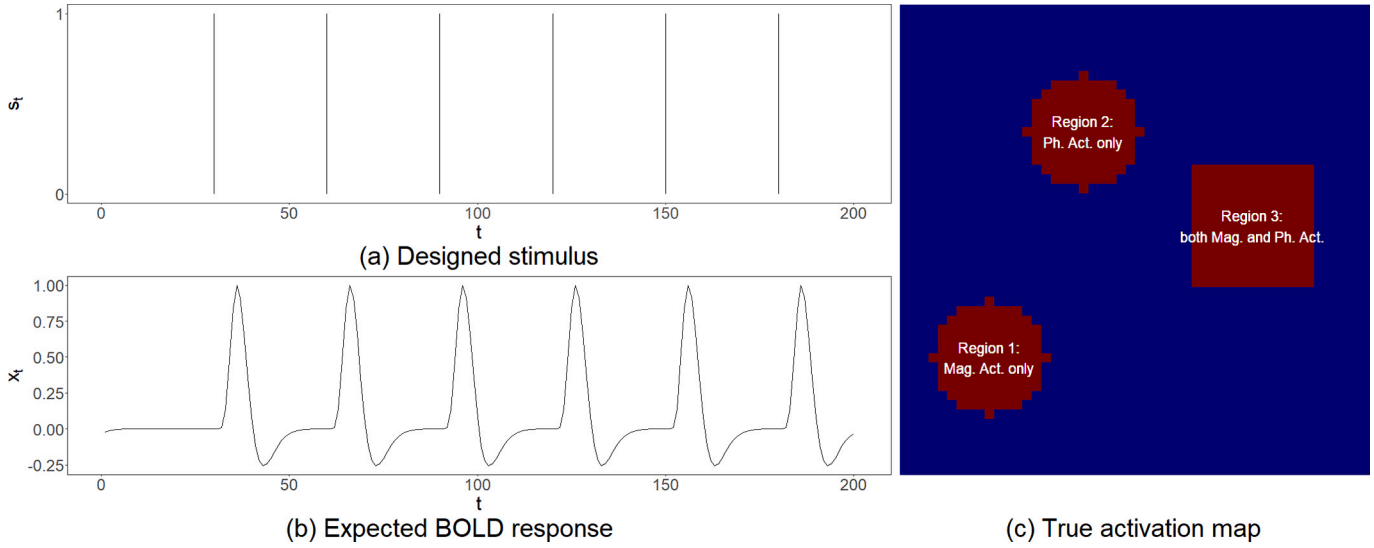

Fig. B.8. (a) Designed stimulus; (b) Expected BOLD response; (c) True activation map for an event-related fMRI simulation study.

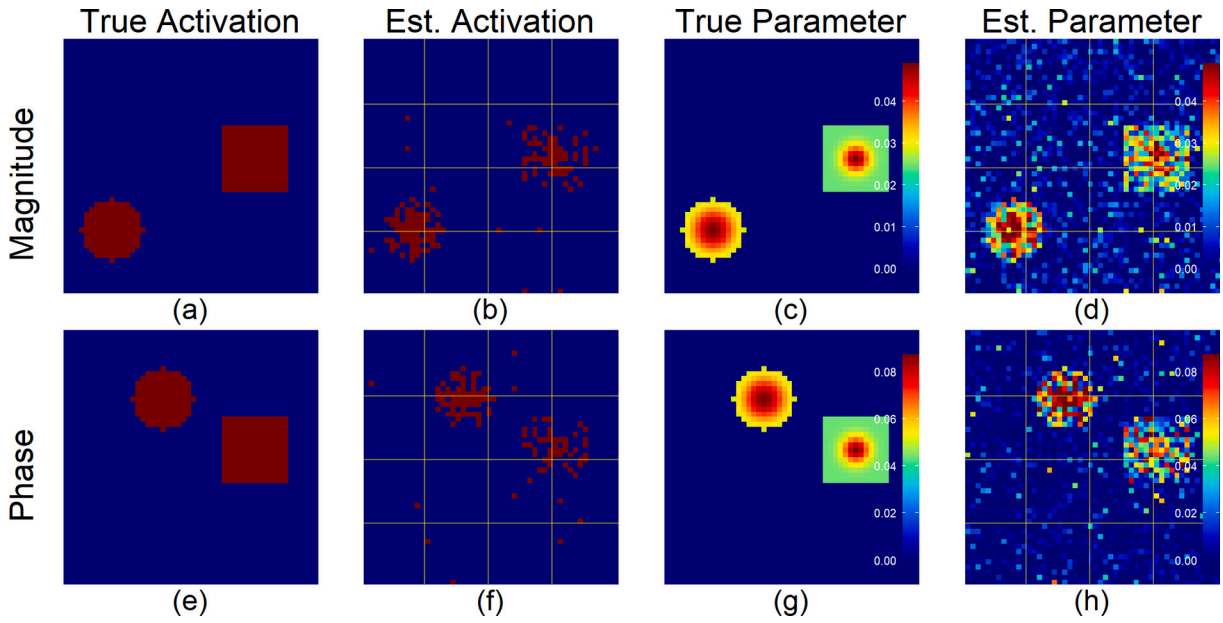

Fig. B.9. (a) and (e) are true magnitude and phase activation maps; (b) and (f) are estimated activation maps as derived from CV-M&P; (c) and (g) are true β_1 and γ_1; (d) and (h) are estimated β_1 and γ_1 as derived from CV-M&P in an event-related fMRI simulation study.

References

[1] Brown RW, Cheng Y-CN, Haacke EM, Thompson MR, Venkatesan R. Magnetic resonance imaging: Physical principles and sequence design. 2nd ed. Hoboken, New Jersey: John Wiley & Sons, Inc.; 2014.

[2] Boynton GM, Engel SA, Glover GH, Heeger DJ. Linear systems analysis of functional magnetic resonance imaging in human V1. J Neurosci 1996;16(13):4207–21.

[3] Logothetis NK. What we can do and what we cannot do with fMRI. Nature 2008;453(7197):869–78.

[4] Rowe DB. Handbook of neuroimaging data analysis, chapter 8. London, United Kingdom: Chapman & Hall; 2019.

[5] Petridou N, Plenz D, Silva AC, Loew M, Bodurka J, Bandettini PA. Direct magnetic resonance detection of neuronal electrical activity. Proc Natl Acad Sci 2006;103(43):16015–20.

[6] Rowe DB, Logan BR. A complex way to compute fMRI activation. NeuroImage 2004;23(3):1078–92.

[7] Feng Z, Caprihan A, K. B. B. c, V. D. Calhoun. Biophysical modeling of phase changes in BOLD fMRI. NeuroImage 2009;47(2):540–8.

[8] Friston KJ, Holmes AP, Worsley KJ, Poline J-P, Frith CD, Frackowiak RSJ. Statistical parametric maps in functional imaging: a general linear approach. Hum Brain Mapp 1994;2(4):189–210.

[9] Lindquist MA. The statistical analysis of fMRI data. Statist Sci 2008;23(4):439–64.

[10] Rice SO. Mathematical analysis of random noise. Bell Syst Tech J 1944;23(3):282–332.

[11] Gudbjartsson H, Patz S. The Rician distribution of noisy MRI data. Magn Reson Med 1995;34(6):910–4.

[12] Rowe DB, Logan BR. Complex fMRI analysis with unrestricted phase is equivalent to a magnitude-only model. NeuroImage 2005;24(2):603–6.

[13] Rowe DB. Modeling both the magnitude and phase of complex-valued fMRI data. NeuroImage 2005;25(4):1310–24.

[14] Rowe DB. Parameter estimation in the magnitude-only and complex-valued fMRI data models. NeuroImage 2005;25(4):1124–32.

[15] Rowe DB, Meller CP, Hoffmann RG. Characterizing phase-only fMRI data with an angular regression model. J Neurosci Methods 2007;161(2):331–41.

[16] Rowe DB. Magnitude and phase signal detection in complex-valued fMRI data. Magn Reson Med 2009;62(5):1356–60.

[17] Adrian DW, Maitra R, Rowe DB. Complex-valued time series modeling for improved activation detection in fMRI studies. Anna Applied Statist 2018;12(3):1451–78.

[18] Lee J, Shahram M, Schwartzman A, Pauly JM. Complex data analysis in high-resolution SSFP fMRI. Magn Reson Med 2007;57(5):905–17.

[19] Yu C-H, Prado R, Ombao H, Rowe DB. A Bayesian variable selection approach yields improved detection of brain activation from complex-valued fMRI. J Am Stat Assoc 2018;113(524):1395–410.

[20] Woolrich MW, Jenkinson M, Brady JM, Smith SM. Fully Bayesian spatio-temporal modeling of fMRI data. IEEE Trans Med Imaging 2004;23(2):213–31.

[21] Musgrove DR, Hughes J, Eberly LE. Fast, fully Bayesian spatiotemporal inference for fMRI data. Biostatistics 2016;17(2):291–303.

[22] Yu C-H, Prado R, Ombao H, Rowe DB. Bayesian spatiotemporal modeling on complex-valued fMRI signals via kernel convolutions. Biometrics 2023;79(2):616–28.

[23] Wang Z, Rowe DB, Li X, Brown DA. Efficient fully Bayesian approach to brain activity mapping with complex-valued fMRI data. arXiv: 2310.18536, available at, https://arxiv.org/abs/2310.18536; 2023.

[24] Rue H, Held L. Gaussian Markov Random Fields. Boca Raton: Chapman & Hall/CRC; 2005.

[25] Gelfand AE, Smith AFM. Sampling-based approaches to calculating marginal densities. J Am Stat Assoc 1990;85(410):398–409.

[26] Rowe DB, Hahn AD, Nencka AS. Functional magnetic resonance imaging brain activation directly from k-space. Magn Reson Imaging 2009;27(10):1370–81.

[27] Nenckaa AS, Hahna AD, Rowe DB. A mathematical model for understanding the statistical effects of k-space (AMMUST-k) preprocessing on observed voxel measurements in fcMRI and fMRI. J Neurosci Methods 2009;181(2):268–82.

[28] Karaman M, Nencka AS, Bruce IP, Rowe DB. Quantification of the statistical effects of spatiotemporal processing of nontask fMRI data. Brain Connect 2014;4(9):649–61.

[29] Mitchell TJ, Beauchamp JJ. Bayesian variable selection in linear regression. J Am Stat Assoc 1988;83(404):1023–32.

[30] Smith M, Fahrmeir L. Spatial Bayesian variable selection with application to functional magnetic resonance imaging. J Am Stat Assoc 2007;102(478):417–31.

[31] Rao SM, Bandettini PA, Binder JR, Bobholz JA, Hammeke TA, Stein EA, et al. Relationship between finger movement rate and functional magnetic resonance signal change in human primary motor cortex. J Cereb Blood Flow Metab 1996;16(6):1250–4.

[32] Epstein R, Kanwisher N. A cortical representation of the local visual environment. Nature 1998;392(6676):598–601.

[33] Reich BJ, Hodges JS, Zadnik V. Effects of residual smoothing on the posterior of the fixed effects in disease-mapping models. Biometrics 2006;62(4):1197–206.

[34] Hughes J, Haran M. Dimension reduction and alleviation of confounding for spatial generalized linear mixed models, journal of the Royal Statistical Society. Series B (Statistical Methodology) 2013;75(1):139–59.

[35] Metropolis N, Rosenbluth AW, Rosenbluth MN, Teller AH, Teller E. Equation of state calculations by fast computing machines. J Chem Phys 1953;21(6):1087–92.

[36] Hastings WK. Monte Carlo sampling methods using Markov chains and their applications. Biometrika 1970;57(1):97–109.

[37] Flegal JM, Haran M, Jones GL. Markov chain Monte Carlo: can we trust the third significant figure? Statist Sci 2008;23(2):250–60.

[38] Welvaert M, Durnez J, Moerkerke B, Berdoolaege G, Rosseel Y. neuRosim: an R package for generating fMRI data. J Stat Softw 2011;44(10):1–18.

[39] R Core Team. R: A Language and Environment For Statistical Computing, R Foundation For Statistical Computing. Vienna, Austria. URL, https://www.R-project.org/; 2023.

[40] Rosen BR, Buckner RL, Dale AM. Event-related functional MRI: past, present, and future. Procced National Acad Sci 1998;95:773–80.

[41] Wilder Penfield EB. Somatic motor and sensory representation in the cerebral cortex of man as studied by electrical stimulation. Brain 1937;60(4):389–443.

[42] Geyer S, Ledberg A, Schleicher A, Kinomura S, Schormann T, Bürgel U, et al. Two different areas within the primary motor cortex of man. Nature 1996;382(6594):805–7.

[43] Culham JC, Valyear KF. Human parietal cortex in action. Curr Opin Neurobiol 2006;16(2):205–12.
[44] Wei W, Zhang K, Chang J, Zhang S, Ma L, Wang H, et al. Analyzing 20 years of resting-state fmri research: trends and collaborative networks revealed. Brain Res 2024;1822:148634. https://doi.org/10.1016/j.brainres.2023.148634.
[45] Kociuba MC, Rowe DB. Complex-valued time-series correlation increases sensitivity in fMRI analysis. Magn Reson Imaging 2016;34(6):765–70.